Available online at www.sciencedirect.com
SCIENCE DIRECT®
Journal of Geodynamics 36 (2003) 633–654
JOURNAL OF GEODYNAMICS
www.elsevier.com/locate/jog

Paleomagnetic analysis of curved thrust belts reproduced by physical models

Elisabetta Costa[a,*], Fabio Speranza[b]

[a]*Dipartimento di Scienze della Terra, Parco Area delle Scienze 157/A, 43100 Parma, Italy*
[b]*Istituto Nazionale di Geofisica e Vulcanologia, Via di Vigna Murata 605, 00143 Rome, Italy*

Received 3 January 2003; received in revised form 20 August 2003; accepted 21 August 2003

Abstract

This paper presents a new methodology for studying the evolution of curved mountain belts by means of paleomagnetic analyses performed on analogue models. Eleven models were designed aimed at reproducing various tectonic settings in thin-skinned tectonics. Our models analyze in particular those features reported in the literature as possible causes for peculiar rotational patterns in the outermost as well as in the more internal fronts. In all the models the sedimentary cover was reproduced by frictional low-cohesion materials (sand and glass micro-beads), which detached either on frictional or on viscous layers. These latter were reproduced in the models by silicone. The sand forming the models has been previously mixed with magnetite-dominated powder. Before deformation, the models were magnetized by means of two permanent magnets generating within each model a quasi-linear magnetic field of intensity variable between 20 and 100 mT. After deformation, the models were cut into closely spaced vertical sections and sampled by means of 1×1-cm Plexiglas cylinders at several locations along curved fronts. Care was taken to collect paleomagnetic samples only within virtually undeformed thrust sheets, avoiding zones affected by pervasive shear. Afterwards, the natural remanent magnetization of these samples was measured, and alternating field demagnetization was used to isolate the principal components. The characteristic components of magnetization isolated were used to estimate the vertical-axis rotations occurring during model deformation. We find that indenters pushing into deforming belts from behind form non-rotational curved outer fronts. The more internal fronts show oroclinal-type rotations of a smaller magnitude than that expected for a perfect orocline. Lateral symmetrical obstacles in the foreland colliding with forward propagating belts produce non-rotational outer curved fronts as well, whereas in between and inside the obstacles a perfect orocline forms only when the ratio between obstacles' distance and thickness of the cover is greater than 10. Finally, when a belt collides with an obstacle in the foreland oblique to the shortening direction the outer front displays rotations opposite in sign to oroclinal-type rotations, whereas the internal fronts seem to assume an "oroclinal type" rotational pattern. Furthermore rotation is easier in

* Corresponding author. Fax: +39-0521-905305.
E-mail addresses: costae@unipr.it (E. Costa), speranza@ingv.it (F. Speranza).

0264-3707/$ - see front matter
doi:10.1016/j.jog.2003.08.003

laterally unconfined models, i.e. when the wedge can "escape" laterally. The results from our models may be useful when compared to paleomagnetic rotations detected in natural arcs. In these cases, our results may allow for better understanding the tectonic setting controlling the genesis of curved mountain fronts, as is the case of the Gela Nappe of Sicily we compare with some of our models.

1. Introduction

Many orogenic belts show curved structural trends in plan view. The kinematics of these belts have been debated in the last decades and curved belts have been generally subdivided in two main end members: oroclines (or rotational arcs) and primary (or non-rotational) arcs. The former are originally straight belts subsequently bent, whereas the latter originated with their curved shape (Carey, 1955; Marshak, 1988). In perfect oroclines there is a 1:1 correlation between paleomagnetic rotation values and deviation of the fold axes from a reference (not rotated) fold axis.

Two kinds of analytical approaches have been used so far to better understand the geological parameters and tectonic settings controlling the development of arcs. First, structural analyses were carried out on curved fronts and paleostress reconstruction was attempted using fault-slip inversion methods (Choukroune, 1969; Angelier, 1979, 1984; Reches, 1987, among many others). More recently, the vertical-axis rotations of different arc-shaped sectors were evaluated by paleomagnetic analyses (Schwartz and Van der Voo, 1983; Eldredge et al., 1985; Hirt and Lowrie, 1988; Speranza et al., 1997; Beck, 1998, among many others). Paleomagnetic analysis has proven to be a useful tool in unraveling the kinematics of arcs, as it is the only technique allowing to discriminate primary arcs from oroclines.

The comparison between paleomagnetic and paleostress data demonstrates that both spatial stress field rotation, induced by previous structures (i.e., faults and other anisotropy of the deforming area), and material rotation can account for the variability of structural trends (Ron et al., 1984, 1993). In principle, accurate paleomagnetic analyses combined with structural investigations should allow to determine the relative contribution of stress field rotation versus material rotation in the formation of arcs. However in actual cases, magnetic mineralogy problems, magnetic overprint, and the poor knowledge of local and regional tectonic settings, due to the lack or scarcity of well exposed and widely distributed structures, have hampered a full comprehension of arc formation processes.

Analogue models have also been used to distinguish between primary, non-rotational arcs and oroclines and used to identify the geological-structural conditions that allow (or prevent) material rotations within a belt (Marshak, 1988; Marshak et al., 1992; Macedo and Marshak, 1999). However, analogue modeling alone does not completely allow detecting material rotations and vertical rotation gradients, but only helps to reconstruct structural trend variations through the deflection of the marker-lines on the model surface.

2. A new modeling methodology

This study proposes a new methodology, which combines physical modeling and paleomagnetic analyses (Magnetized Analog Modeling) with the aim of unraveling the connection between tectonic

settings, deformation and material rotations in thin-skinned arcs. Our models were designed following the tectonic settings used in various models by Marshak (1988) and Marshak et al. (1992) with the aim of comparing their and our results. Thus, the present study deals only with modeling reproducing settings that are reported in the literature to give rise to oroclines, without comparing the models to any particular natural example, except for one setting, which has been compared to the Gela Nappe of the Maghrebian thrust belt of Sicily (Italy). For this reason our models were scaled down by a length factor $L^* \approx 2 \times 10^{-6}$, which is intermediate between the two scaling factors mainly used in physical modeling, i.e. 1×10^{-5} and 1×10^{-6} (1 cm in the models reproduces 1 and 10 km, respectively). This scaling factors allowed us to reproduce natural settings large enough to give general ideas without overcome the size of thin skinned thrust belts.

2.1. Modeling procedures

A series of experiments (11, of which two undeformed and 9 deformed models) were performed at the Lab of Dipartimento di Scienze della Terra dell'Università di Parma (Italy) to test the influence of different factors on kinematics and rotation patterns. The models were prepared using dry quartz sand or sand and glass micro-beads mixed with 0.5% (weight) of magnetite powder (Table 1). These materials have shown to be good analogues of the shallow crust in thin-skinned tectonics (Hubbert, 1951; Davis et al., 1983; Mulugeta, 1988; Vendeville et al. 1987; Krantz, 1991; Schellart, 2000, among many others). Some experiments were run with the same features using alternatively different kinds of basal detachments, because bending in thin-skinned tectonics is, at least partly, a consequence of differential displacements on the basal detachment of the deforming wedge (Gwinn, 1967). We used frictional detachments as well as viscous décollements, reproduced by silicone layers underlying the frictional cover, to model salt or over-pressurized shale tectonics. This allowed us to test the influence of both rheology and frictional strength at the base of deforming wedges on rotations. Frictional basal detachments were obtained by covering the sandbox floor with plastic sheets. In these cases the coefficient of basal friction $\mu_b = 0.47$ (Storti and McKlay, 1995). Viscous basal décollements were obtained by interposing between the sand layers and the sandbox floor a silicone layer (Dow Corning silicone gel with viscosity of 10^4 Pa s^{-1} at room temperature; Table 1). Shortening was performed by moving a rigid wall continuously at various velocities depending on the rheology of basal detachments: $v = 2$ cm/h for models having frictional basal detachments, $v = 3$ mm/h for models with viscous basal décollements. In fact, unlike brittle rocks, whose strength depends on the applied stress, viscous materials (i.e. rock salt and the silicone used in our models to reproduce the behavior of

Table 1
Mechanical and physical properties of the materials used in the models

Materials	Density (g/cm^3)	Max. grain size (μm)	Angle of internal friction φ	Dynamic shear viscosity η (Pa s)
Sand	1.75	300	30°	–
Silicone	0.976	–	–	2×10^4
Glass micro-beads		300	15.7°	–
Magnetite		300	–	–

such rocks) have a strength that increases with increasing strain rate. The wall was moved at constant velocities by an electronically controlled motor and stopped when an average 30% bulk shortening was attained.

Our models were designed to reproduce simple and generic situations and, thus, have not been scaled down to particular natural settings (Table 2). We modeled arcs formed by: (a) pushing an indenter into the model and (b) the interaction with various kinds of obstacles in the foreland. Indenters refer to rigid masses or backstops that push into the deforming body, while obstacles refer to any feature that restrains the forward propagation of an orogenic wedge (Marshak et al., 1992).

Some models had rigid lateral walls to reproduce deformation occurring at lower structural levels where the deforming mass is laterally confined. Some other models were only partly laterally confined (semi-confined) and some others completely laterally unconfined, to reproduce deformation at either intermediate or shallow structural levels, where the deforming mass is increasingly more free to shift laterally when shortened under the applied stress.

Pictures were taken at fixed time intervals both of top and lateral views to reconstruct the kinematics of deformation.

2.2. Paleomagnetic analysis

Before being deformed, the models were subjected to a magnetic field reaching the maximum intensity of 100 mT produced by two permanent magnets located at the model edges, normal to the shortening direction (Fig. 1). The magnets were removed before deformation. After deformation the models were consolidated, cut in various cross sections and then sampled for paleomagnetic analyses at key positions using Plexiglas cylinders 1.0 cm in diameter and 1.0 cm in height (Fig. 2). We sampled only gently dipping thrust sheets carefully avoiding strongly deformed areas (thrust

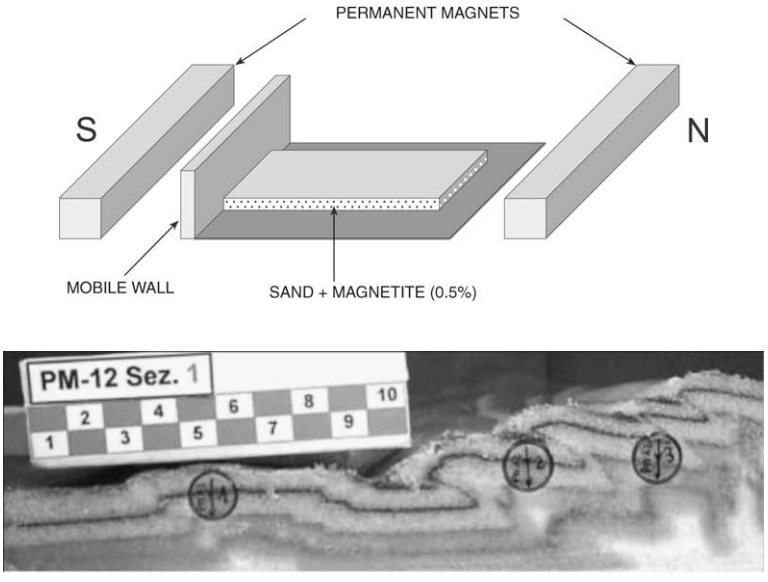

Fig. 2. Example of sampling along a cross section cut in one of the deformed models. The Plexiglas cylinders are 1.0 cm in diameter and 1.0 cm in height.

Table 2
Characteristics of the models

	Mod. N°	2	8	9	10	12	13	14	15	16
Models features		Ob.(30°) Ins. Obstacle Unconf.	Lat. symm. Obstacle X = 15 cm	Ob.(30°) Ins. Obstacle Conf.	Ob.(30°) sur.. Obstacle Conf.	Ob.(45°) sur.. Obstacle Conf.	indenter	Lat. symm. Obstacle X = 22cm	indenter	Ob.(30°) Ins. Obstacle Unconf
Dimensions (cm) L. (max-min)xWxT.		28-17x20x2	50x35x2	28-17x20x2	40x33x2	40x33x2	40x35x2	50x35x2	40x35x2	28-17x20x2
Materials		sand	Sand+micro-beads	Sand+micro-beads	Sand+micro-beads	Sand+micro-beads	Sand+micro-beads	Sand+micro-beads	Sand+silicone	Sand+silicone
Detachment		Frictional	Frictional	Frictional	Frictional	Frictional	Frictional	Frictional	Viscous	Viscous
Ob = oblique; sur = surmountable; ins = Insurmountable; lat.symm. = lateral symmetrical; conf. = confined; unconf. = unconfined										

surfaces, fold hinges, recumbent folds). In this way two problems potentially invalidating the paleomagnetically-determined vertical-axis rotations were avoided: first, the larger the bedding dip, the less defined the magnetic declination and, second, rocks which underwent high internal strain (such as shear zones), show paleomagnetic vector significantly deflected (e.g. Borradaile, 1993).

It must also be considered that sand is a non-cohesive material that is only slightly affected by compaction during deformation, which is achieved at room pressure and temperature. In these conditions the grains of sand, and hence also the magnetite grain, do not suffer any pervasive strain that could deflect the remanence vector (Borradaile and Mothersill, 1989). The location of each sample was determined using the walls of the sandbox as co-ordinates: in this way, vertical and horizontal axis rotations induced in the models by deformation could be reconstructed at every given point. The N–S direction relative to the induced field is parallel to the shortening direction, i.e. any horizontal magnetic vector parallel to the shortening direction will have magnetic declination (D) = 0 and inclination (I) = 0 values.

The remanent magnetization of the samples was measured by a 2G cryogenic magnetometer in the shielded room of the paleomagnetic laboratory at the Istituto Nazionale di Geofisica e Vulcanologia, Roma.

The samples were magnetically cleaned by alternating field up to a maximum intensity of 100 mT, and the remanence was measured after each demagnetization step. Magnetization components were evaluated on orthogonal demagnetization diagrams by principal component analysis (Kirschvink, 1980).

Different demagnetization diagrams were observed depending on the distance of the sample from the magnets (i.e. the N–S model edges). In samples located close to the model edges, a single magnetization component was isolated and eliminated at 80–100 mT (Fig. 3a). In samples located farther from the model edges, a single component of magnetization is observed after 4 mT and eliminated at 50 mT (Fig. 3b). Finally, at the center of the model, where the weakest magnetic field is induced, the samples exhibit a low-coercivity component (carrying approximately 90% of the total remanence) eliminated at about 20 mT, and a randomly oriented higher-coercivity component which is demagnetized at 50–100 mT (Fig. 3c). This implies that at the center of the model, at a distance of about 15–20 cm from the magnets, the induced magnetic field did not exceed the value of 20 mT. The magnetic fraction reoriented by the permanent magnets (and subsequently demagnetized) has a 20–100 mT coercivity, typical for magnetite. For some representative samples we performed the isothermal remanent magnetization (IRM) acquisition curves using a pulse magnetizer with a maximum field of 2.7 T. These curves show that the 90–100% of saturation occurs at 200 mT, confirming that a low-coercivity mineral (magnetite) is present in the magnetic powder. The samples were found to be very strongly magnetized: close to the model walls the natural remanent magnetization (NRM) was as high as several A/m (Fig. 3a), whereas progressively decreasing NRM intensities were observed moving towards the center of the model. Here the NRM values were about 1/100 than those measured close to the model walls (Fig. 3c).

The measured declinations (Table 3) are plotted on the top view of the various deformed models as arrows whose color defines the vertical position of the samples (i.e. white = samples collected in deeper thrust sheets, black = samples collected in shallower thrust sheets). The vertical-axis rotations occurring during model deformation are obtained by comparing the declination values to the N–S direction: positive and negative declination values represent clockwise (CW) and counterclockwise (CCW) rotations, respectively.

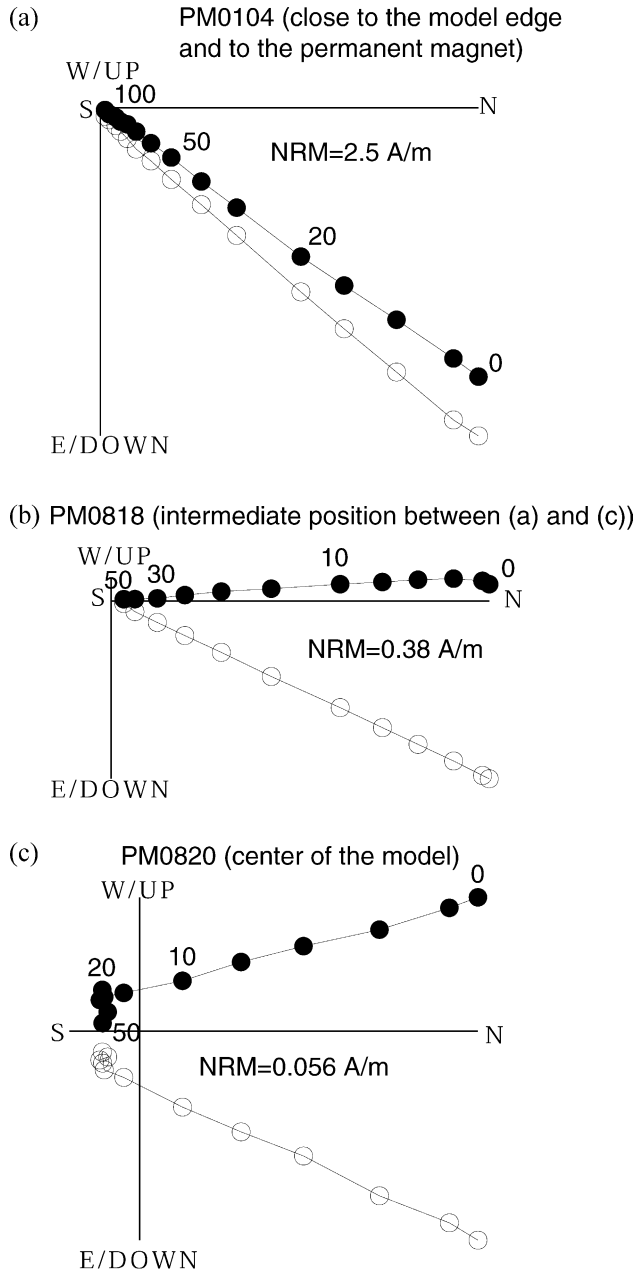

Fig. 3. Vector diagrams of typical alternating magnetic field (AF) demagnetization data from samples coming from different distances from the magnets (and the model edges), geographic coordinates. Demagnetization step values are in millitesla. Open and solid circles represent projections on the vertical and horizontal planes, respectively. NRM, natural remanent magnetization. See text for further explanation.

Table 3
Declination values: positive = CW rotations; negative = CCW rotations

Sample no.:	1	2	3	4	5	6	7	8	9	10	11	12	13	14	15	16	17	18	19	20	21	22	23
Model no.																							
2	– –	−63	−11	29	20	6	36	−22															
3	3	6	−1	3	7	0	−17	13	4	−4	−5	6	3	9	−1	−1	−3	−7					
4	0	1	−11	1	1	−12	0	11															
8	0	18	−6	21	37	3	−8	−5	2	9	7	−4	30	−19	4	6	−24	−3	−1	−15	−76	−50	−16
9	12	13	18	10	−9	– –	−7	−4	2	6	12	12	0	12	−14	−15							
10	−18	9	−6	−7	−20	−27	−10	−13	1	0	1	6	9	16	17	16							
12	9	−17	−18	14	−9	−7	1	−3	6	−1	1	5	2	2	7	12							
13	10	11	62	0	14	4	1	10	−20	– –	9	−4											
14	−1	36	11	6	25	17	−5	13	−1	30	23	5	−4	0	−27	−19	−7	−48	−19				
15	1	21	4	−15	0	9	19	17	2	−7	−7	−13	−24	−54	1	−19	−2	−21	−40				

To check whether the observed magnetic declinations represent vertical-axis material rotations instead of local deflections of the magnetic field lines generated by the permanent magnets (i.e. that the models were correctly N–S magnetized), two magnetized models (Models 3 and 4) were sampled before deformation. The pre-deformation declinations were shown to be always $<10^\circ$ and mostly $<5^\circ$ (Fig. 4a). Significant deflections are located only close to the magnet lateral borders and are CW at the NW–SE corners and CCW at the NE–SW corners, respectively. In order to minimize the above mentioned border effect, the width of the models was always kept smaller than the magnet length. Consequently, the local deflections of the magnetic field lines must be considered as small ($<5^\circ$) and negligible compared to the material vertical axis rotations.

After deformation, the samples exhibit rotations that can be related to material rotations (Fig. 4b). Our models deform mainly by thrusting. The cohesion drop occurring along faults formed in sand models (Krantz, 1991) allows thrust-sheets to overthrust their footwalls without significant deformation of the constituting material, except for frontal gentle fault-bend folds. This occurs in particular when vertical normal stress and basal shear strain are low, as in our models having maximum thickness up to 2 cm and coefficient of basal friction, $\mu_b = 0.47$. In the samples coming from fault-related folds the inclinations deviate from the 0–25° values (typical of the undeformed model) to more steep values generally positive. This clearly reflects the formation of folds and strata steepening in the frontal part of thrust sheets. The declination values of samples showing large I values ($>50^\circ$) were considered as barely significant, because they imply subvertical and strongly deformed strata, where declination is not defined. As our purposes were to assess the results only as qualitative data, we will consider the movement of thrust-sheets as passive and the rotations detected as passive rotations.

2.3. Limitations of the method

Our analogue modeling is more useful for generating new concepts and stimulating new ideas than for giving quantitative results. Moreover the models we designed represent generic structural settings, thus the results we obtained must be considered as merely qualitative.

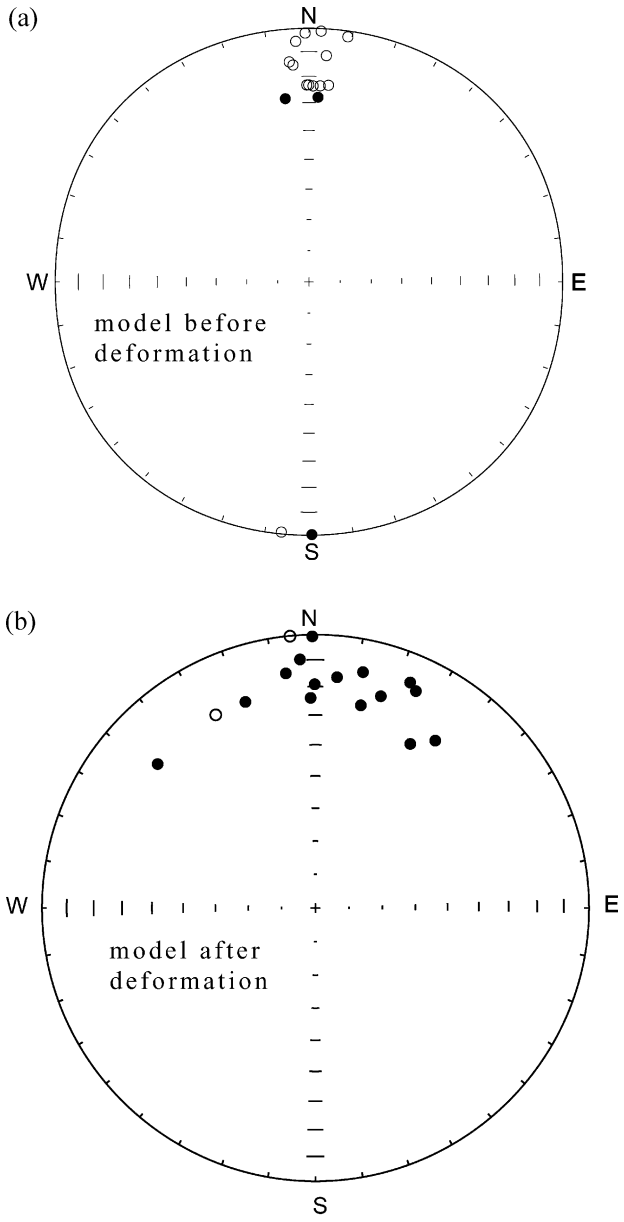

Fig. 4. Equal-area projections of the paleomagnetic directions from two analogue models. Open (solid) circles represent projection onto the upper (lower) hemisphere. Directions in (a) are from an undeformed model, and are parallel to the field lines produced by the two permanent magnets used to magnetize the models. Directions in (b) are from a deformed model and deviate from those shown in (a) due to vertical- and horizontal-axis rotations occurring during model deformation.

The scaling factor for lengths applied in our models is $L^* \approx 2 \times 10^{-6}$. The 2.2 × 2.5-cm size of cylindrical paleomagnetic samples from natural outcrops would imply in models a sample size of the dimension of few grains of sand. But the size of our samples is $\cong 1$ cm^3 and cannot be further reduced for technical problems. This implies that the rotations detected in each sample

taken in the various models can in principle represent the algebraic sum of the rotations detected in a huge rock mass in nature. However this is not dramatic in the models, as we completely control their deformation evolution. This allows us to take each sample in an evenly deformed area (i.e. a single thrust sheet) and avoid the shear zones so that the possibility that the rotation detected in a sample is the algebraic sum of opposite rotations is minimized. Moreover we studied models reproducing curved orogens, which are large-scale tectonic features, where rotations should be of the same sign and amount for tens of km along the same thrust sheet. For all the above reasons we estimate that, to study this particular problem (belt bending), the impossibility to scale the samples took in the models to normal paleomagnetic cores does not change the overall results.

3. Experiments

3.1. Indenters

We reproduced curved thrust belts due to indenters by pushing a vertical mobile wall into one of the edges of the models (Fig. 5 and Table 2). In model 13 the sand sheet deformed above a

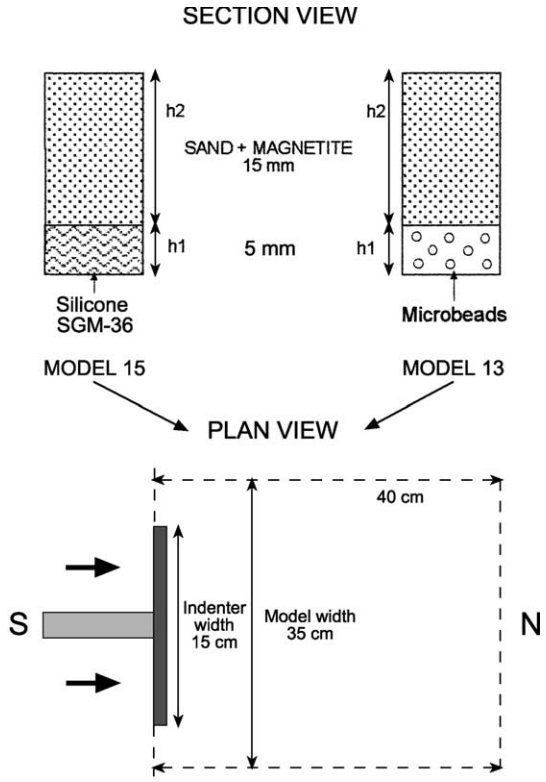

Fig. 5. Scheme showing the features of Models 13 and 15, both in plan and section views. The models differ only for the basal detachment layer: frictional in the former and viscous in the latter.

basal frictional detachment ($\mu_b = 0.47$), i.e. a plastic sheet covering the base of the sandbox. On the contrary, in model 15 the sand sheet deformed above a basal viscous layer made of silicone (Table 1). All the other features were the same in the two models except the shortening velocity that was of 2 cm/h in Model 13 and 3 mm/h in Model 15 (see Section 2.1).

3.1.1. Results

In both models the outer curved front shows small and scattered rotations (Fig. 6). Conversely, the more internal fronts in both models show rotations coherent with the oroclinal model, although smaller than the oroclinal-type expected rotations (Eldredge et al., 1985).

We conclude that indenters do not produce either oroclines or a non-rotational arcs (terminology of Marshak, 1988), but complex arcs. Small and random rotations are observed in the outer front, and oroclinal-type rotations in the more internal thrusts, although their magnitude is smaller with respect to a perfect orocline.

3.2. Obstacles

Various models with different kinds of stationary obstacles in the foreland were designed to reproduce various natural situations (Table 2). They model, in a simplified way, the presence of

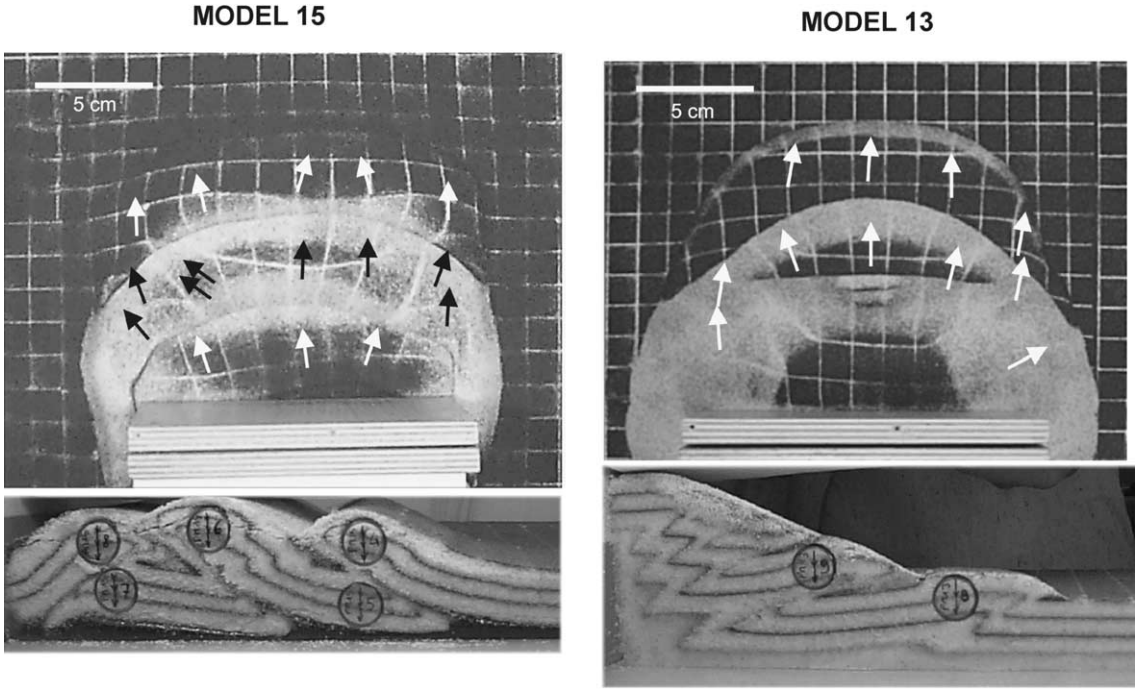

Fig. 6. Plan and section views of the Models 13 and 15 after deformation. Arrows indicate the paleomagnetic declinations, i.e. the rotations due to tectonics, measured from samples. To ensure an optimum vision either black or white arrows are used respectively on light and dark backgrounds. The vertical profiles show that, in models detaching on viscous layers, backthrusting prevails on forethrusting. The diameter of Plexiglas cylinders is 1 cm.

seamounts, basement culminations in inverted basins, lateral transition between basin and shelf carbonates etc. The obstacles were either surmountable or insurmountable to reproduce respectively shallow and deep portions of the deforming sheets.

3.2.1. Lateral symmetrical obstacles

Two models were constructed (Model 8 and 14; Table 2) having two 6 cm-diameter Plexiglas cylinders, variably spaced apart, representing obstacles in the foreland (Fig. 7). These obstacles, whose thickness exceeded the models' thickness, could represent stratigraphic pinch-outs of weaker basal horizons, seamounts or basement massifs entering subduction (Marshak et al., 1992). Both models were made of sand and micro-beads (frictional behavior) detaching on the base of the sandbox covered by a plastic sheet ($\mu_b = 0.47$) and were laterally unconfined. The micro-beads, weaker than the sand, allow the deforming front to advance easier and faster. The only feature changing in the two models was the spacing between the two cylinders (X in Fig. 7), which tested whether shape variations correspond to different amounts of rotations. Macedo and Marshak (1999) argued that the wider the spacing the smaller the degree of protrusion of the frontal arc.

3.2.1.1. Results. The rotations measured in the two models show substantial differences (Fig. 8). In Model 14, having more distant obstacles, the more internal fronts display orocline-type rotations, whereas in Model 8 they show irregular rotations. Moreover, both models do not show any systematic rotation in the outer thrust front. Therefore these models show that when a forward propagating orogenic wedge collides with two obstacles, the outermost and youngest thrust front is a non-rotational arc (as also proposed in absence of paleomagnetic measurements by Macedo and Marshak, 1999). On the contrary, the internal thrust fronts located in-between and inside the

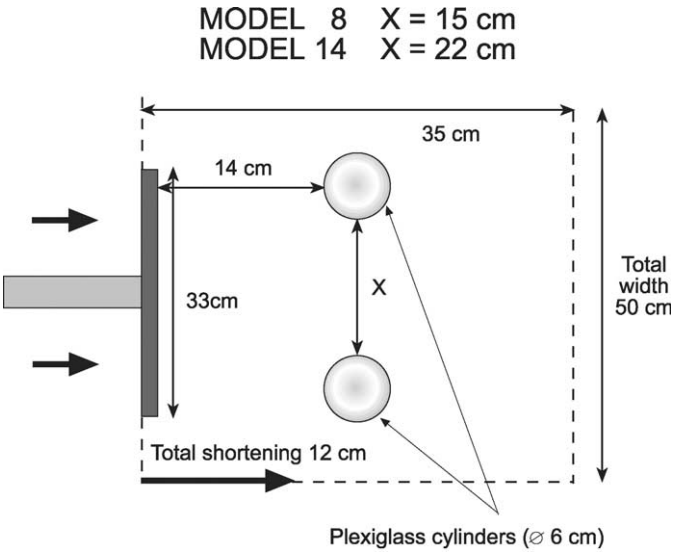

Fig. 7. Scheme of Models 8 and 14. The only difference between the two models is the separation X between the two obstacles. See text for further explanation.

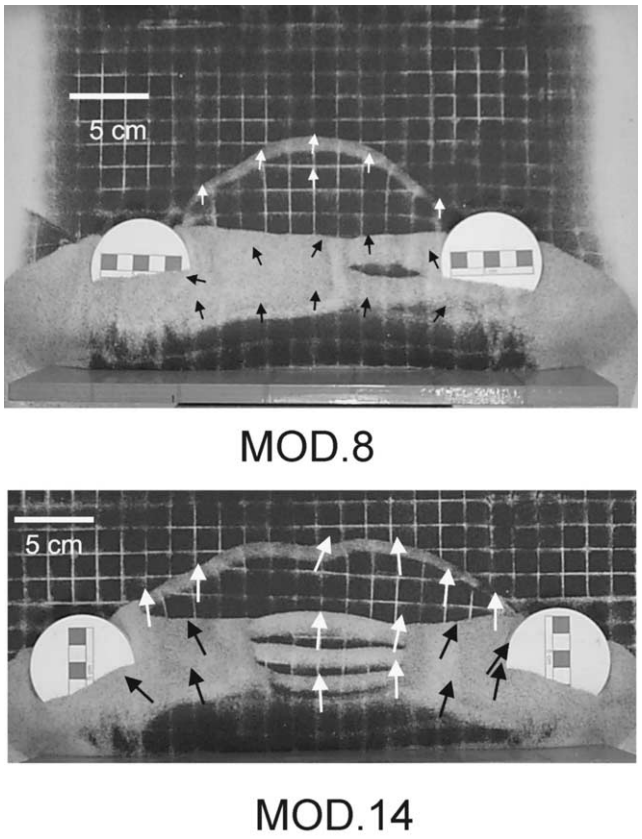

Fig. 8. Plan view of the Models 8 and 14 after deformation. Arrows indicate the rotations due to tectonics. Symbols as in Fig. 6.

obstacles form an orocline only when the distance between the obstacles (X) is nearly 10 times larger than the thickness of the deforming sequence (h), i.e. $R = X/h \geqslant 10$. This experimental value could be better constrained when further experiments are run.

3.2.2. Obstacles in the foreland oblique to the shortening direction

We designed six models (Models 2, 9, 10, 12 and 16; Fig. 9) to test the influence on rotation of different factors combined to oblique obstacles. The presence of an obstacle in the foreland oblique to the shortening direction is the feature common to all six models.

Model 10 had a surmountable obstacle and was laterally semi-confined. Both Models 2 and 9 had insurmountable obstacles but they were laterally unconfined and confined, respectively. The different lateral confinements try to model the different behavior of thrust sheets forming at either shallow or deep levels in thin-skinned tectonics. In this way we tested whether the structural level of the deforming sheets influences vertical rotations.

3.2.2.1. Insurmountable obstacles. We compared the rotations obtained in Model 2 to those obtained in Model 9, which both had the same features except for lateral confinement (Fig. 9a).

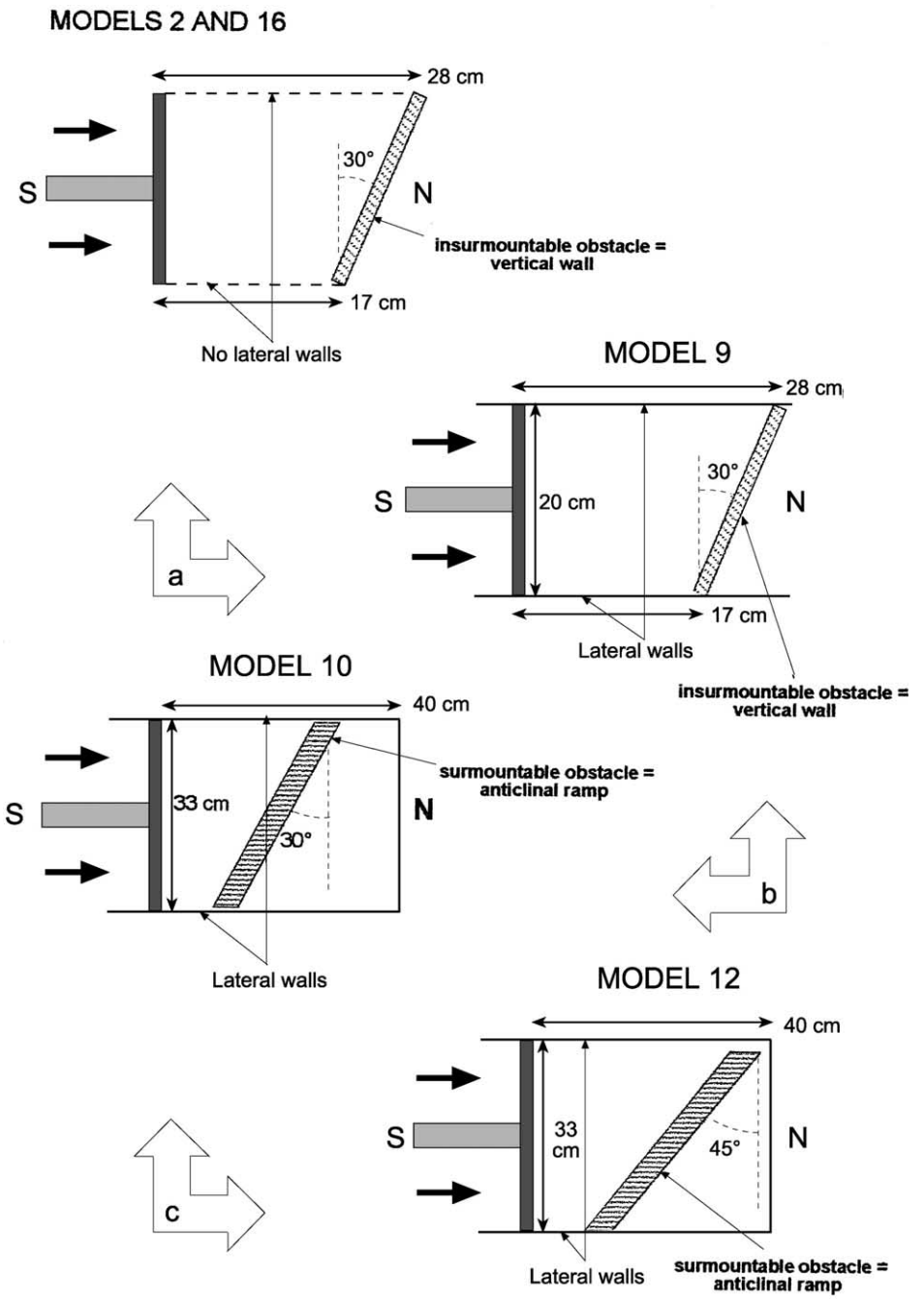

Fig. 9. Scheme showing and comparing the various features of: (a) Models 2 and 9; (b) Models 9 and 10; (c) Models 10 and 12. The variables are: the lateral confinement, the surmountability of the obstacle and the able between the obstacle and the shortening direction. See text for further explanation.

3.2.2.2. Results. In model 2 (Fig. 10) the part directly impacting the obstacle (right frontal part) shows CCW rotation. This part is forced to move away from the obstacle during shortening provoking a CCW material rotation. On the contrary, the dextral shear component along the obstacle is likely to be confined within a very thin slice of sand along the obstacle itself. The CW rotation shown by the left frontal portion of the model could then be due to the dextral shear component along the obstacles, although, near to the obstacles, the strain paths are likely to be even more complex. In Model 9, which is laterally confined, the part directly impacting the obstacle is almost non-rotated. This is due to the possibility of mass movement in the laterally unconfined models. The more internal thrust-sheets, which do not impact the obstacle, show a gentle radial pattern of rotation due to the lateral drag that occurs at the contact between the shortening central portion and the stationary lateral parts of the models. The rotation trend shown by the more internal thrust-sheets is common to all models of our, that propagate forward by a piggyback thrust sequence.

3.2.2.3. Surmountable obstacles. Models 9 and 10 had the same features (i.e. they are laterally confined) except for the surmountability of the obstacle (Fig. 9b).

3.2.2.4. Results. The rotations detected in the two models are very small and quite similar (Fig. 11). This demonstrates that lateral confinement has the greatest influence on rotation impeding any lateral shift caused either by the right shear component along the obstacle or by the left mass movement away from the obstacle. Applying this result to natural settings would imply that rotations mainly occur in thrust sheets deforming at shallow structural levels, as in Model 2.

Also in Model 10 the more internal fronts show a gentle radial pattern of rotation due to the lateral simple shear.

3.2.2.5. Obliquity of the obstacle. Models 10 and 12 have the same characteristics (i.e. they are laterally confined and have surmountable oblique obstacles) except for the angle between the obstacle and the shortening direction that is of 60° in Model 10 and of 45° in Model 12 (Fig. 9c).

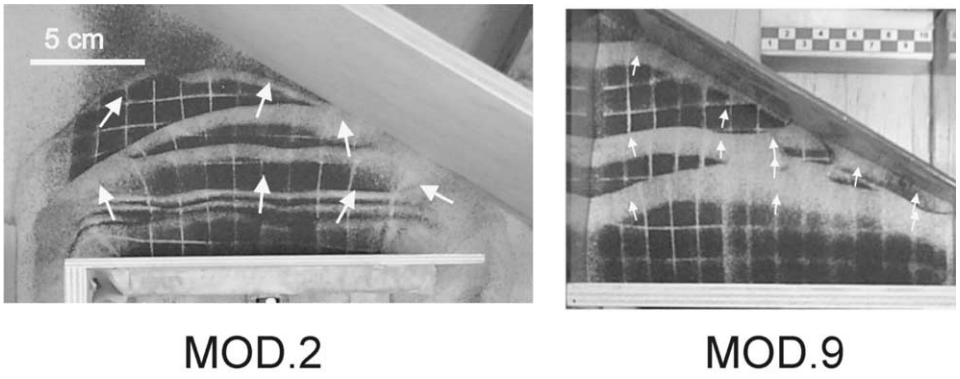

Fig. 10. Plan view of Models 2 and 9 after deformation. The diffrence between the two models is the lateral confinement. Model 2 is laterally unconfined whereas lateral walls confine model 9. Arrows indicate the rotations due to tectonics. Symbols as in Fig. 6.

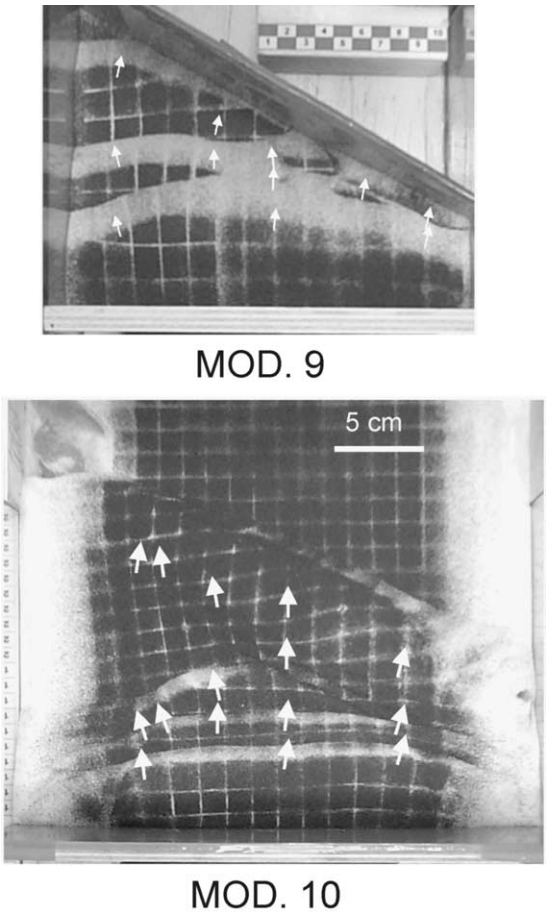

Fig. 11. Plan view of Models 9 and 10 after deformation. In Model 9 the wedge impact an insurmountable obstacle whereas in Model 10 a surmountable obstacle. Arrows indicate the rotations due to tectonics. Symbols as in Fig. 6.

These two models were compared to test whether the obliquity of the obstacle to the shortening direction influences either the trend or the amount of rotation.

3.2.2.6. Results. The rotations documented in the two models are small and quite similar although the shape of the two fronts is very different. In Model 12, the front located just inside the most external one shows a curved shape at its center. Surprisingly, also this part of the front, trending normal to the obstacle, shows no significant rotations as well as the last, more external front (Fig. 12).

Here, as well as in other models, it is shown that rotation of marker lines on top surface of models not always match with vertical material rotation. Either differential motion along small, closely spaced vertical fault surfaces parallel to the movement vector or sliding of the shallowest layer of sand possibly causes this mismatch. It is also possible that rotation does not propagate to the shallowest sheet of sand, which does not directly impact the surmountable obstacle, due to the negligible cohesion of the sand.

Also in this case, the lateral confinement seems to play a major role on rotations that are small in both models whereas the more internal fronts show a gentle radial pattern of rotation due to the lateral simple shear.

3.2.2.7. Rheology of basal detachments. To test whether the rheology of basal detachments plays a role on rotations, two models were run having the same features (i.e. insurmountable obstacles in the foreland oblique to the shortening direction and no lateral confinement) except for the basal detachment (Fig. 9a). Model 2 detaches at the interface between the micro-beads and the plastic sheet covering the base of the sandbox. This frictional detachment has a coefficient of basal friction $\mu_b = 0.47$. Model 16 has a basal décollement made of a silicone viscous layer.

3.2.2.8. Results. The rotations shown by the two models have similar overall trends—i.e. CW and CCW rotations at the left and right parts of the outer fronts, respectively, and CCW rotations at the left lateral part of the more internal fronts (Fig. 13). On the contrary the amount of rotation is quite different and apparently contradictory in the two models. The rotations occurring at the outer front are greater in the model having a frictional basal detachment (Model 2 in Fig. 13). Conversely, rotations occurring at the internal fronts are greater in the model with a viscous basal décollement (Model 16 in Fig. 13).

This can be explained as follows. In the model with a basal viscous décollement thrusting advances faster and farther than in the one having a frictional basal detachment (Costa and Vendeville, 2002, and references therein). This behavior accounts for an increased lateral shear that, in turn, favors oroclinal-type rotations at the lateral termination of the older and more internal thrust sheets. Furthermore, when pushed from behind, the viscous basal layer tends to spread radially. This behavior of the décollement layer opposes to the rotation trends shown by

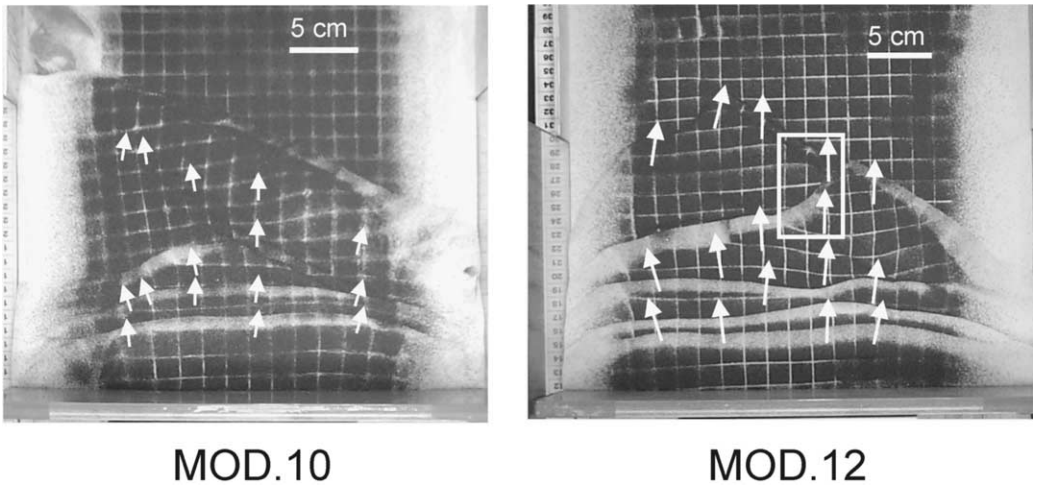

Fig. 12. Plan view of Models 10 and 12 after deformation. The two models have the same characteristics except the angle between the obstacle and the direction of forward propagation of the wedge: 30° in Model 10 and 45° in Model 12. Arrows indicate the rotations due to tectonics, whereas the rectangle delimitates the rotated front. Symbols as in Fig. 6.

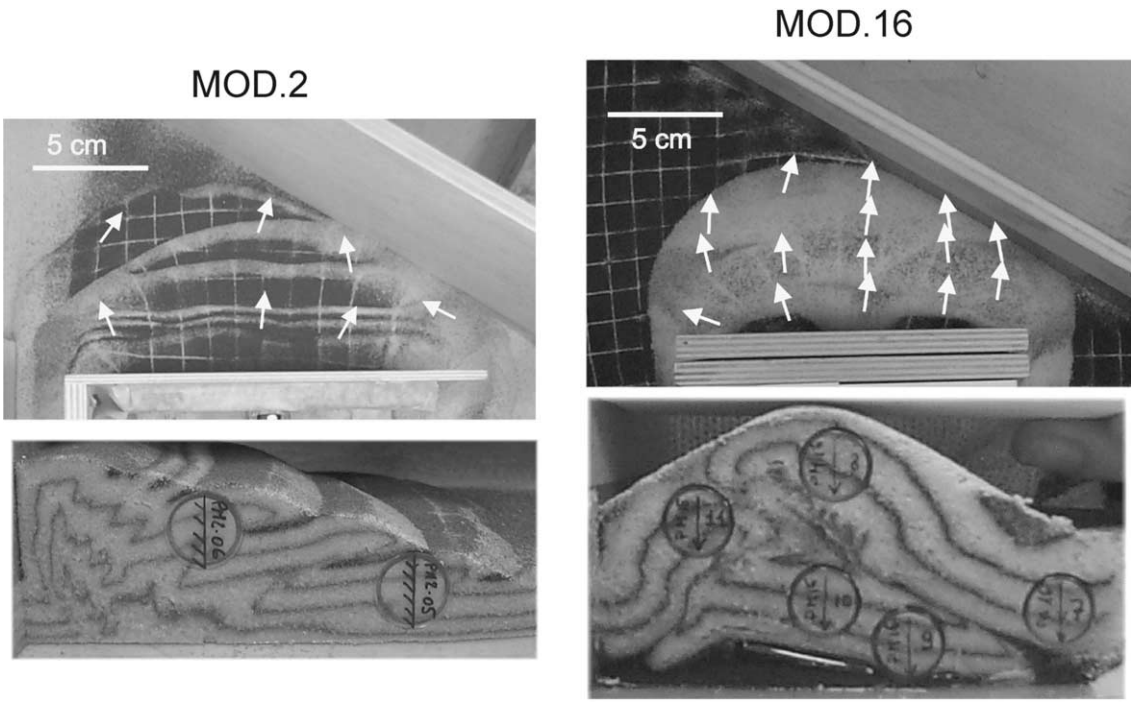

Fig. 13. Plan and section views of Models 2 and 16 after deformation. The two models have the same characteristics except the rheology of the basal detachment: frictional in Model 2 and viscous in Model 16. Arrows indicate the rotations due to tectonics. Also in this case the vertical profiles show that, in models detaching on viscous layers, backthrusting prevails on forethrusting. The diameter of Plexiglas cylinders is 1 cm. Symbols as in Fig. 6.

the outer front, as described above. The above mentioned reasons explain the occurrence of both a greater shear strain component at the lateral end of the internal thrusts and a reduced rotation at the outer front shown in Model 16.

It is however noteworthy that in both models the outer front shows rotations opposite in signs to the oroclinal model, i.e. CW and CCW in the left and right arc limb, respectively.

4. Natural examples

As it has been said before, our models were designed to reproduce simple and generic situations and, thus, were not designed to reproduce particular natural settings.

Only the results of the models dealing with lateral symmetrical obstacles have been compared with a natural example of this setting, which may be represented by the Gela Nappe of the Maghrebian thrust belt of Sicily. The Gela Nappe is a striking, southward-verging, salient corresponding to the largest southward advancement of the Sicilian Maghrebian belt over the African foreland (Fig. 14). It is formed by a thin-skinned wedge exposing upper Miocene-mid Pleistocene basinal sediments (Lickorish et al., 1999). Though deformation seems to have stopped during mid Pleistocene times, ongoing N–S shortening is documented by borehole stress-in-situ

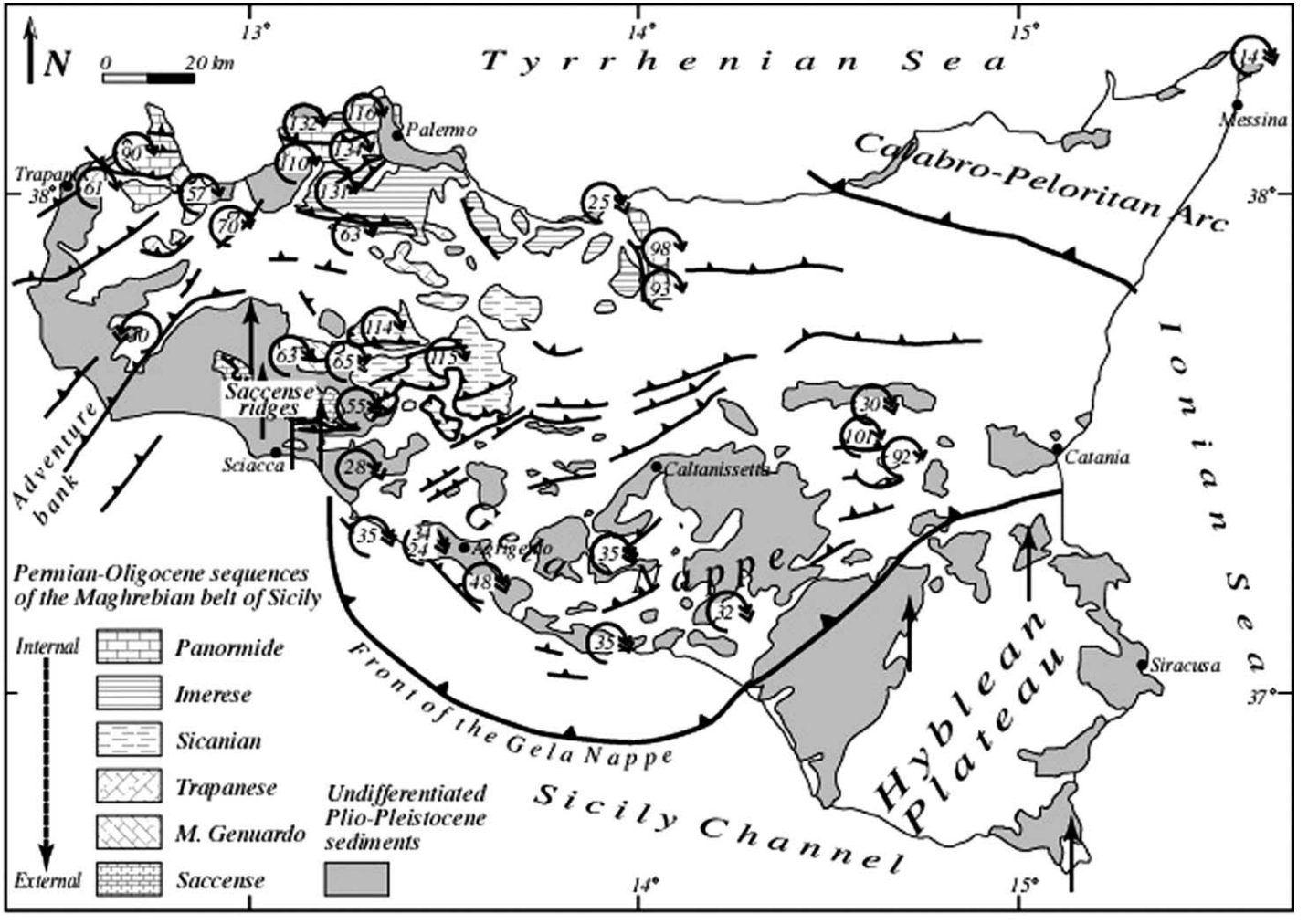

Fig. 14. Schematic map of Sicily and paleomagnetic orogenic rotations (see Speranza et al., 2003, for details on data). Vertical arrows indicate unrotated areas. Circular arrows (and the enclosed angle) indicate the amount of clockwise and counterclockwise rotations calculated for the single sampling localities. Circular arrows with simple and double tips indicate results from Mesozoic-Palaeogene and Neogene rocks, respectively. Mesozoic-Palaeogene and Neogene rotations are calculated by comparing the obtained palaeodeclinations to the coeval expected African directions and to the geocentric axial dipole (GAD) field direction, respectively. Note the regional pattern of clockwise rotations, which are uniform all over the Gela Nappe salient, where no local arc-related rotation is observed.

data (Ragg et al., 1999). The Gela Nappe salient develops between two uplifted domains exposing thick and rigid shelf carbonates: the Hyblean plateau to the east, and the Saccense ridges to the west (Fig. 14). These two platform carbonate domes may have represented the foreland obstacles colliding with a southward propagating thrust wedge and causing the formation of a pronounced belt salient.

Paleomagnetic studies have shown that in Sicily large-scale CW rotations occurred synchronous with thrust sheet development (Channell et al., 1990; Speranza et al., 1999, 2003). CW rotations seem to have a regional character, and to be genetically related with the spreading of the southern Tyrrhenian Sea, which induced the formation of a large-scale orocline represented by southern Apennines, Calabria, and Sicilian Magherbides belt fragments (e.g. Gattacceca and Speranza, 2002; Speranza et al., 2003). In Sicily, Speranza et al. (2003) have shown that a 70° CW rotation occurred in mid Miocene times, followed by a late Miocene-Pleistocene 30° CW rotation. Plio-Pleistocene sediments sampled in several parts of the Gela Nappe show invariantly 10–30° CW rotations (Channell et al., 1992; Scheepers and Langereis, 1993; Speranza et al., 1999, 2003, Fig. 14). Older pre-orogenic sediments exposed at the edges of the Gela Nappe itself similarly show a ubiquitous 100° total orogenic rotation, without any major difference between the eastern and western limbs of the salient (Channell et al., 1990; Speranza et al., 2003).

The paleomagnetic data summarized above show that the Gela Nappe salient is an almost perfect non-rotational arc, once the uniform CW rotation of the Sicilian nappes is eliminated. This evidence from a natural setting is in complete agreement with the results of our analogic models, showing that lateral symmetrical obstacles in the foreland colliding with forward propagating wedges produce a non-rotational outer curved front.

5. Conclusions

This study shows that arcs formed by (a) indenters, (b) lateral symmetrical obstacles in the foreland, and (c) obstacles oblique to the shortening direction, develop distinct patterns of rotations of paleomagnetic vector. 1. Indenters pushing into deforming wedges form non-rotational curved outer fronts (Models 13 and 15); they are almost perfect non-rotational arcs.

2. Lateral symmetrical obstacles in the foreland colliding with forward propagating wedges produce non-rotational outer curved fronts as well, located farther beyond the obstacles, as is also shown by the Gela Nappe of Sicily. In-between and behind the obstacles a perfect orocline forms only when the ratio between obstacles' distance and cover thickness is greater than 10.

3. Deforming wedges colliding with obstacles in the foreland, oblique to the shortening direction, display rotations of the outer fronts opposite in sign to the oroclinal rotations.

4. The more internal fronts rotate only later, due to both lateral shear strain and interaction with later and more external fronts. They show oroclinal rotations, but the magnitude of rotation is smaller than that expected for a perfect orocline, except for those fronts formed inside the lateral symmetrical obstacles.

5. When deforming wedges collide with obstacles, rotations most strongly affect laterally unconfined wedges. Also in thin-skinned tectonics of natural settings rotations are probably easier where rocks are poorly confined laterally or on the upper side, i.e. in the shallower structural levels.

6. Viscous basal décollements favor radial rotations in the older and more internal thrust-sheets. On the contrary they smooth over rotations occurring close to the obstacles. Both the above features are due to the radial path of flowage of viscous layers.

This study represents a first step to better understand, by means of paleomagnetic analysis carried out on analogue models, the kinematics of arcs and the evolution of oroclines in different tectonic settings. Our results show that rotations detected in deformed models are influenced by many diverse factors that often are not completely known in natural settings. Thus, paleomagnetic data from models compared to those from natural arcs might give new insights on kinematics as well as on depth, rheology and strength of basal detachment and presence of blind obstacles. Magnetized Analog Modeling can thus help to unravel the tectonic settings responsible for the formation and evolution of different arc-shaped fronts.

Acknowledgements

This study was strongly encouraged by Gianpaolo Pialli, who unfortunately passed away before its conclusion; for this reason we would like to dedicate it to our lost friend. We are also grateful to Giorgio Ranalli for generous help and scientific support and to Keith Benn, whose revision greatly improved the paper.

References

Angelier, J., 1979. Determination of the mean principal directions of stress for a given fault population. Tectonophysics 56, 17–26.

Angelier, J., 1984. Tectonic analysis of fault slip data set. J. Geophys. Res. 89, 5835–5848.

Beck, M.E., 1998. On the mechanism of crustal block rotations in the central Andes. Tectonophysics 299, 75–92.

Borradaile, G.J., 1993. The rotation of magnetic grains. Tectonophysics 221, 381–384.

Borradaile, G.J., Mothersill, J., 1989. Tectonic strain and Paleomagnetism: experimental investigation. Physics of the Earth and Planetary Interiors 56, 254–265.

Carey, W., 1955. The orocline concept in geotectonics. Pap. Proc. R. Soc. Tasmania 89, 255–289.

Channell, J.E.T., Oldow, J.S., Catalano, R., D'Argenio, B., 1990. Paleomagnetically determined rotations in the western Sicilian fold and thrust belt. Tectonics 9 (4), 641–660.

Channell, J.E.T., Di Stefano, E., Sprovieri, R., 1992. Calcareous plankton biostratigraphy, magnetostratigraphy and palaeoclimatic history of the Plio-Pleistocene Monte San Nicola section (southern Sicily). Bollettino della Società Paleontologica Italiana 31, 351–382.

Choukroune, P., 1969. Un example d'analyse microtectonique d'une serie calcaire affectee de plis isopaque (concentrique). Tectonophysics 7, 57–70.

Costa, E., Vendeville, B.C., 2002. Experimental insights on the geometry and kinematics of fold-and-thrust belts above weak, viscous evaporitic decollement. Journal of Structural Geology 24, 1729–1739.

Davis, D., Suppe, J., Dahlen, F.A., 1983. Mechanics of fold and thrust belts and accretionary wedges. J. Geophys. Res. 88, 1153–1172.

Eldredge, S., Bachtadse, V., Van der Voo, R., 1985. Paleomagnetism and the orocline hypothesis. Tectonophysics 119, 153–179.

Gattacceca, J., Speranza, F., 2002. Paleomagnetism of Jurassic to Miocene sediments from the Apenninic carbonate platform (southern Apennines, Italy): evidence for a 60° counterclockwise Miocene rotation. Earth Planet. Sci. Lett. 201, 19–34.

Gwinn, V., 1967. Curvature of marginal folded belts flanking major mountain ranges: Accented or caused by lateral translation of epidermal stratified cover? Spec. Pap. Geol. Soc. Am. 115, 1–87.
Hirt, A.M., Lowrie, W., 1988. Paleomagnetism of the Umbrian-Marches orogenic belt. Tectonophysics 146, 91–103.
Hubbert, M.K., 1951. Mechanical bases for certain familiar geologic structures. Geol. Soc. Am. Bull. 62, 355–372.
Kirschvink, J.L., 1980. The least-square line and plane and the analysis of paleomagnetic data. Geophys. J. R. Astron. Soc. 62, 699–718.
Krantz, R.W., 1991. Measurements of friction coefficients and cohesion for faulting and fault reactivation in laboratory models using sand and sand mixtures. Tectonophysics 188, 203–207.
Lickorish, W.H., Grasso, M., Butler, R.W.H., Argnani, A., Maniscalco, R., 1999. Structural styles and regional tectonic setting of the "Gela Nappe" and frontal part of the Maghrebian thrust belt in Sicily. Tectonics 18, 655–668.
Macedo, J., Marshak, S., 1999. Controls on the geometry of fold-thrust belt salients. Geol. Soc. Am. Bull. 111, 1808–1822.
Marshak, S., 1988. Kinematics of orocline and arc formation in thin-skinned orogens. Tectonics 7 (1), 73–86.
Marshak, S., Wilkerson, M.S., Hsui, A., 1992. Generation of curved fold-thrust belts: Insights from simple physical and analytical models. In: McClay, K.R. (Ed.), Thrust Tectonics. Chapman and Hall, London, pp. 59–90.
Mulugeta, G., 1988. Modelling the geometry of Coulomb thrust wedges. Journal of Structural Geology 10 (8), 847–859.
Ragg, S., Grasso, M., Muller, B., 1999. Patterns of tectonic stress in Sicily from borehole breakout observations and finite element modelling. Tectonics 18, 669–685.
Reches, Z., 1987. Determination of the tectonic stress tensor from slip along faults that obey the Coulomb yeld condition. Tectonics 6, 849–861.
Ron, H., Freund, R., Garfunkel, Z., 1984. Block rotation by strike-slip faulting: structural and paleomagnetic evidence. J. Geophys. Res. 89 (B7), 6259–6270.
Ron, H., Nur, A., Aydin, A., 1993. Stress field rotation or block rotation: an example from the Lake Mead fault system. Annali di Geofisica XXXVI (2), 65–73.
Scheepers, P.J.J., Langereis, C.G., 1993. Analysis of NRM directions from Rossello composite: Implications for tectonic rotations of the Caltanissetta basin, Sicily. Earth Planet. Sci. Lett. 119, 243–258.
Schellart, W.P., 2000. Shear test results for cohesion and friction coefficients for different granular materials: scaling implications for their usage in analogue modelling. Tectonophysics 324, 1–16.
Schwartz, S.Y., Van der Voo, R., 1983. Paleomagnetic evaluation of the orocline hypothesis in the central and southern Appalachians. Geophys. Res. Lett. 10, 505–508.
Speranza, F., Sagnotti, L., Mattei, M., 1997. Tectonics of the Umbria-Marche-Romagna Arc (central northern Apennines, Italy): new paleomagnetic constraints. J. Geophys. Res. 102, 3153–3166.
Speranza, F., Maniscalco, R., Mattei, M., Di Stefano, A., Butler, R.W.H., Funiciello, R., 1999. Timing and magnitude of rotations in the frontal thrust system of southwestern Sicily. Tectonics 18 (6), 1178–1197.
Speranza, F., Maniscalco, R., Grasso, M., 2003. Pattern of orogenic rotations in central-eastern Sicily: implications for the timing of spreading in the Tyrrhenian Sea. Journal of the Geological Society, London 160, 183–195.
Storti, F., McKlay, K., 1995. Influence of syntectonic sedimentation on thrust wedges in analogue models. Geology 23, 999–1002.
Vendeville, B., Cobbold, P.R., Davy, P., Brun, J.P. and Choukroune, P., 1987. Physical models of extensional tectonics at various scales. In: Coward, M.P., Dewey, J.F., Hancock, P.L. (Eds.), Continental Extensional Tectonics. Spec. Publ. Geol. Soc. 28. Geological Society, London, pp. 95–107.